Plastic Deformation Behavior of Aluminum Casting Alloys A356/357

Q.G. WANG

The plastic deformation behavior of aluminum casting alloys A356 and A357 has been investigated at various solidification rates with or without Sr modification using monotonic tensile and multiloop tensile and compression testing. The results indicate that at low plastic strains, the eutectic particle aspect ratio and matrix strength dominate the work hardening, while at large plastic strains, the hardening rate depends on secondary dendrite arm spacing (SDAS). For the alloys studied, the average internal stresses increase very rapidly at small plastic strains and gradually saturate at large plastic strains. Elongated eutectic particles, small SDAS, or high matrix strength result in a high saturation value. The difference in the internal stresses, due to different microstructural features, determines the rate of eutectic particle cracking and, in turn, the tensile instability of the alloys. The higher the internal stresses, the higher the damage rate of particle cracking and then the lower the Young's modulus. The fracture strain of alloys A356/357 corresponds to the critical amount of damage by particle cracking locally or globally, irrespective of the fineness of the microstructure. In the coarse structure (large SDAS), this critical amount of damage is easily reached, due to the clusters of large and elongated particles, leading to alloy fracture before global necking. However, in the alloy with the small SDAS, the critical amount of damage is postponed until global necking takes place due to the small and round particles. Current models for dispersion hardening can be used to calculate the stresses induced in the particles. The calculations agree well with the results inferred from the experimental results.

I. INTRODUCTION

WITH the current demand of weight reduction for improved product performance and fuel economy, aluminum casting alloys A356/357 are increasingly being used in critical structural applications in automotive and aerospace industries such as engine blocks, cylinder heads, chassis, suspension systems, *etc*. As many of these applications involve high stresses, the plastic deformation and tensile properties of the alloys are critical in both design and manufacturing.

The tensile properties and fracture behavior of cast aluminum alloys A356 and A357 strongly depend on the microstructure, which is simply comprised of age-hardenable aluminum dendritic matrix, mainly strengthened by Mg/Si precipitates,[1] and a dispersion of eutectic silicon and Fe-rich intermetallic particles. The initial yield stress is largely determined by the Mg/Si precipitates in aluminum matrix formed during aging. The large strain behavior, however, involves a strong interaction of plastic flow with eutectic silicon and Fe-rich intermetallic particles that locate in aluminum dendritic cell and grain boundaries (Figures 1 and 2).[2] The tensile fracture of alloys A356 and A357 is initiated by the cracking of eutectic silicon[3,4–8] and Fe-rich intermetallic[9–13] particles due to high tensile stresses induced by plastic deformation in the aluminum matrix. In both A356 and A357, the number of cracked particles increases nearly linearly with the plastic strain.[6–12] Cracked particles serve as nucleation sites for voids that eventually lead to fracture of the alloys.[3–5,8–13]

The fracture of eutectic particles during plastic deformation suggests a very efficient load shedding mechanism from the deforming matrix onto the undeformable eutectic particles. For alloy A356, the damage process and tensile behavior can be rationalized using theories of dispersion hardening.[7,11] The predicted strain hardening rates follow the predictions of Brown–Stobbs's model[14,15] when plotted as a function of the particle aspect ratio at low strains and SDAS at large strains. The Bauschinger effect is also dependent on both aspect ratio and SDAS as predicted according to the particle dislocation interaction.[7,16] Particle cracking follows quite well the predictions of the Brown–Stobbs' model, *i.e*., particle stresses increase with plastic strain, following the predicted strain hardening rate for different aspect ratio and SDAS. Nevertheless, for larger and more elongated particles, the probability of cracking seems to reach a saturation limit, suggesting that the direct proportionality of particle stresses to particle aspect ratio is probably excessive.[7] For alloy A357, the population of eutectic particle size and aspect ratio is also different from that of A356 alloy due to the increased Fe-rich (mainly π phase) intermetallic particles. In the present work, the plastic deformation behavior of both A356 and A357 alloys with various microstructures has been quantified in terms of the development of internal stresses shed onto the eutectic particles, the Young's modulus, and the tensile instability during plastic deformation. A Be-free version of alloy A357 was used in the study to make the effect of Fe-rich intermetallics more evident as well as to

Q.G. WANG, formerly Doctoral Student, Co-operative Research Center for Cast Metals Manufacturing (CAST), The University of Queensland, Brisbane, Queensland, Australia, is Senior Materials Engineer, Advanced Materials Engineering, Powertrain, General Motors Corporation, Pontiac, MI 48340-2920. Contact e-mail: Qigui.Wang@gm.com

This article is based on a presentation given in the symposium "Dynamic Deformation: Constitutive Modeling, Grain Size, and Other Effects: In Honor of Prof. Ronald W. Armstrong," March 2-6, 2003, at the 2003 TMS/ASM Annual Meeting, San Diego, California, under the auspices of the TMS/ASM Joint Mechanical Behavior of Materials Committee.

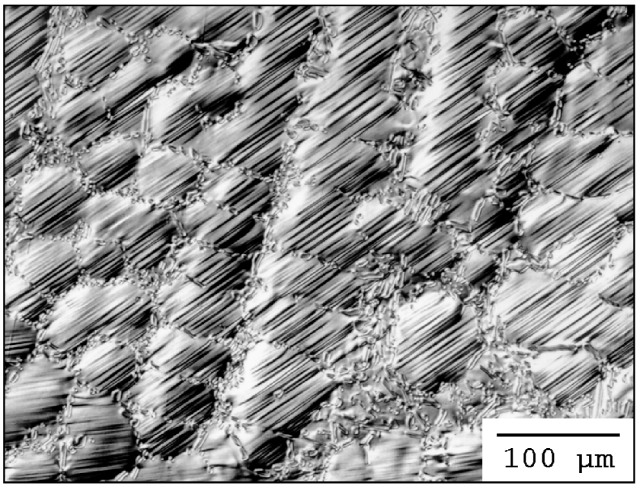

Fig. 1—Nomarski-contrast micrograph showing the interaction between slip bands and eutectic particles on the cell boundaries in a sample with large SDAS (56 μm). Applied strain: 1 pct; Alloy: A357, unmodified.[2]

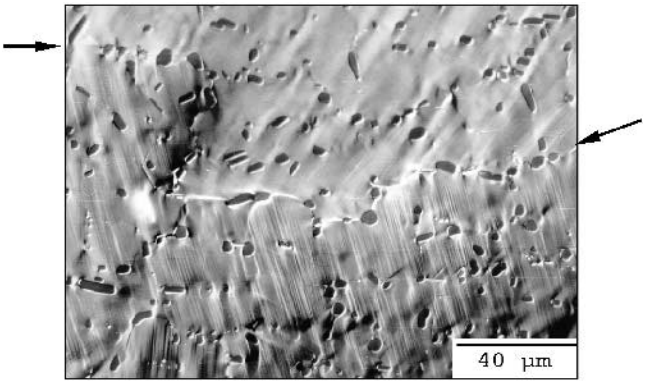

Fig. 2—Nomarski-contrast micrograph showing the interaction between slip bands and a grain boundary (identified by the arrows) in a sample with small SDAS (17 μm). Applied strain: 2.3 pct; Alloy: A357, unmodified.[2]

facilitate the quantitative metallography. The particle stresses were calculated based on the current models for dispersion hardening and compared with the results concluded from the Bauschinger testing. The results complement those from previous studies on Al-7Si-0.4–0.7Mg alloys.[2,6–12,16]

II. THEORETICAL FRAMEWORK

A. *Tensile Stress Induced in the Eutectic Particles during Plastic Deformation*

Metals often exhibit a decrease in the reverse yield stress when they are deformed cyclically. This, so-called Bauschinger effect, is usually intercepted in terms of the internal stresses induced by inhomogeneous deformation.[7,17–20] The Bauschinger stress parameter (BSP) is defined in terms of the forward and reverse flow stresses, σ^f and σ^r, as shown in Figure 3, after some applied plastic prestrain:[7,17]

$$\text{BSP} = \frac{\left|\sigma^f\right| - \left|\sigma^r\right|}{\left|\sigma^f\right|} = 2\frac{\sigma_b}{\sigma^f} \qquad [1]$$

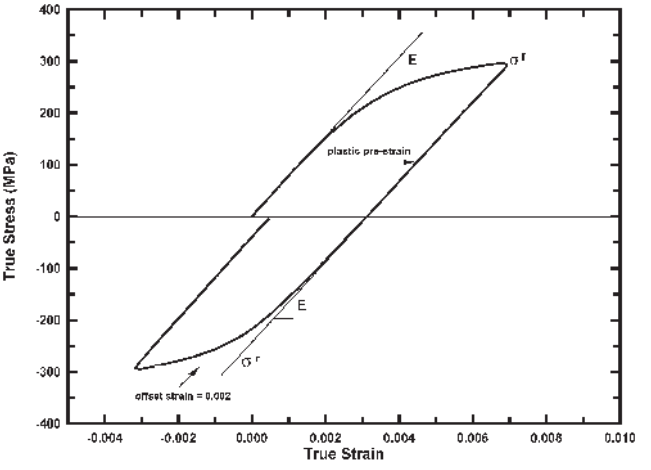

Fig. 3—Bauschinger cycle with the plastic prestrain and the forward σ^f and reverse σ^r stresses defined.

where σ^r is measured at an arbitrarily chosen offset plastic strain (equal to 0.002). The term σ_b is the mean back stress, which the particles exert on the dislocations in the matrix.

The dispersed hard particles, such as silicon and Fe-rich intermetallic particles in alloys A356 and A357, affect the strain hardening through two different processes: particle-induced long-range internal stress, which increases linearly with the unrelaxed plastic strain around uncracked particles, and a parabolic hardening due to short-range internal stress.[14,15,19,21] Of these two internal stresses, the long-range internal stress was reported to be associated with the low strain ($<$1 pct) hardening, which is independent of the particle size, and depends only on the volume fraction of particles, plastic strain, and particle aspect ratio.[7,21,22] After straining continues beyond about 1 pct, the shear dislocation array ceases to be stable, and gives way to the prismatic arrays. At this stage, the long-range stresses do not disappear, but they grow much less rapidly than before. Prismatic loops contribute to this long-range stress, but more importantly, they introduce a series of short-range stress peaks into the region between particles. These appear to control the subsequent stages of the stress-strain curve.[21] Figure 1 shows the interaction between slip bands and eutectic particles in the cell boundaries in an A357 alloy.

The long-range internal stress (σ_l) is directional in character; that is, if the straining direction is reversed, it aids plastic flow, while parabolic short-range stress is nondirectional and always opposes plastic flow.[7,20–22] Accordingly, the forward and reverse flow stresses can be written as

$$\sigma^f = \sigma_{YS} + \sigma_{sf} + \sigma_l \qquad [2]$$

$$\sigma^r = \sigma_{YS} + \sigma_{sr} - \sigma_l \qquad [3]$$

where σ_{YS} is initial flow stress equal to yield stress; σ_{sf} is forward short-range internal stress; σ_{sr} is reverse short-range internal stress; and σ_l is a directional component. Based on Eq. [1], the back stress σ_b induced by particles in the material is given as

$$\sigma_b = \frac{\sigma^f - \sigma^r}{2} = \frac{2\sigma_l + \sigma_{sf} - \sigma_{sr}}{2} \qquad [4]$$

1. *Long-range internal stress*

Suppose that the matrix containing the undeformable particles undertakes a symmetrical plastic shear strain, γ. Following Brown,[23] Brown and Clarke,[22] and Cáceres *et al*.,[7] the uniform shear stress generated in the particles, τ_p, can be given as

$$\tau_p = 2\varphi\beta\mu_m\gamma^* \quad [5]$$

where γ^* is the unrelaxed plastic strain, which is equal to γ in the low strain regime; φ is an "accommodation factor" equal to the elastic strain in the particle divided by the plastic strain in the matrix. The term φ depends on the morphology of particles and the slip system of the matrix, and is equal to 0.393 for spheres and 0.75 for plates in a matrix deforming by multiple slip.[22] The β is the modulus correction factor to account for elastic inhomogeneity. For flake particles, the modulus correction factor β is given as[22]

$$\beta = \frac{\mu_p}{\mu_m} \quad [6]$$

whereas for small spherical particles, β is determined by[22]

$$\beta = \frac{\mu_p}{\mu_p - \varphi(\mu_p - \mu_m)} \quad [7]$$

The terms μ_m and μ_p are the shear moduli of the matrix and particles, respectively. For silicon particles in aluminum, $\mu_p = 80$ GPa and $\mu_m = 26.2$ GPa; thus, β is equal to 1.34 and 3.54 for spherical and flake particles, respectively.

Followed Brechet *et al*.[24] and Cáceres *et al*.,[7] it is supposed that the shear stress in the particles, τ_p, is also a function of particle aspect ratio α^a, where the exponent a is a number between 0 and 1. Assuming that eutectic particles in A356 and A357 alloys are a mixture of equal quantity of spherical and flake particles ($\varphi = 0.57$; $\beta = 2.44$; and $a = 0.5$), the shear stress can be rewritten as

$$\tau_p = 2.8\sqrt{\alpha}\,\mu_m\gamma^* \quad [8]$$

and tensile stress $\sigma_p(\alpha)$ is given by

$$\sigma_p = 2\tau_p = 5.6\sqrt{\alpha}\,\mu_m\gamma^* \quad [9]$$

The total long-range internal stress σ_l in the matrix, generated by a volume fraction of uncracked particles (f_{uc}), can be defined as

$$\sigma_l = 5.6 f_{uc}\sqrt{\alpha}\,\mu_m\varepsilon^* \qquad (\varepsilon^* \le \varepsilon_c^*) \quad [10]$$

where ε^* is unrelaxed tensile strain ($\varepsilon^* = \gamma^*$); and ε_c^* is the upper limit for the no plastic relaxation regime.

2. *Short-range internal stress*

With the increase of strains (>1 pct), plastic relaxation and particle cracking takes place, which significantly decreases the strain hardening and the rate of accumulation of stresses in the particles. The long-range internal stress is no longer dominant in the hardening. In contrast, the short-range internal stress, due to the accumulation of forest dislocations including geometrically necessary dislocations and statistically stored dislocations, further contributes to strain hardening. According to Brown and Stobbs,[14,15] Hansen,[25] and Cáceres *et al*.,[7] the generation of forest dislocations around the particles, due to secondary slip, has two effects. First, it hardens the matrix directly and makes relaxation progressively more difficult, inhibiting the local slip required to relieve the elastic energy. Second, it results in an increase in the elastic loading on the particles, and a concomitant increase in the image stress. Therefore, the short-range internal stress is the sum of geometrically necessary dislocation hardening stress, σ_g, statistically stored dislocation hardening stress, σ_s, and image stress, σ_i.

a. *Geometrically necessary dislocation hardening stress*

The geometrically necessary dislocations are the dislocations necessary to avoid overlaps or voids around the particles in cell or grain boundaries. According to Ashby[21] and Hansen,[25] the contribution to the forest hardening from the geometrically necessary dislocations is given as

$$\sigma_g = C\mu_m\sqrt{\frac{C_1 b}{l}(\varepsilon - \varepsilon_c^*)} \quad [11]$$

where b is the magnitude of the Burgers vector of the dislocations, C and C_1 are constants, and l is the geometric slip distance.

In the A356 and A357 alloys, the eutectic silicon particles and Fe-rich intermetallics are not uniformly distributed as in the "normal" dispersion-hardened materials but are clustered along the dendrite cell boundaries and interdendritic regions. The density of eutectic particles in the cell boundaries plays an important role in the deformation and fracture behavior.[2] The cell boundary with a dense eutectic particle wall, acting as a grain boundary, divides the microstructure into many isolated regions. The dislocations can continuously slip only within the dendrite cell and are blocked in the cell boundaries (Figure 1). In the finer SDAS structure, however, the cell boundary become less distinct and more open and thus the dislocations can slip across several dendrite cells and finally stop at the grain boundaries (Figure 2). In this case, the use of SDAS as the geometric slip distance may not be strictly valid particularly for the finest SDAS structure. However, the grain size may not be a good measure either, since some dislocations will be stopped by particles within the grain. For simplicity, the SDAS, λ, has also been used as the geometric slip distance in the finer structure in this work.

b. *Statistically stored dislocation hardening stress, σ_s*

In general, the statistically stored dislocations are accumulated during uniform deformation (matrix hardening). The contribution of statistically stored dislocations to the matrix hardening is given as[21,25]

$$\sigma_s = C\mu_m\sqrt{\frac{C_2 b}{L}(\varepsilon - \varepsilon_c^*)} \quad [12]$$

where L is the average dislocation slip distance in the matrix, and C and C_2 are constants. According to Hansen[25] and Cáceres *et al*.,[7] for aluminum alloys, $C \approx 1.25$ and $C_2/L \approx 0.05\ \mu\text{m}^{-1}$.

c. *Image stress*

According to Brown and Stobbs,[14,15] the image stress is an additional stress induced by forest dislocation interaction, which is $\sqrt{f_{uc}}$ times the forest dislocation hardening

itself. Based on the preceding analysis, the image stress is given as

$$\sigma_i = \sqrt{f_{uc}}(\sigma_g + \sigma_s) = C\sqrt{f_{uc}}\mu_m\sqrt{b\left(\frac{C_1}{\lambda} + \frac{C_2}{L}\right)(\varepsilon - \varepsilon_c^*)} \quad [13]$$

Like long-range internal stress, the image stress is directional in character. It results in a decrease in the reverse flow stress by a factor of $2\sqrt{f_{uc}}$ compared with the forward flow stress it produced.

Accordingly, the flow stresses in both forward and reverse directions are given by

$$\sigma^f = \sigma_{YS} + 5.6 f_{uc}\sqrt{\alpha}\,\mu_m\varepsilon^* \qquad (\varepsilon^* \le \varepsilon_c^*) \quad [14a]$$

$$\sigma^f = \sigma_{YS} + 5.6 f_{uc}\sqrt{\alpha}\,\mu_m\varepsilon_c^* + C\left(1 + \sqrt{f_{uc}}\right)\mu_m \sqrt{b\left(\frac{C_1}{\lambda} + \frac{C_2}{L}\right)(\varepsilon - \varepsilon_c^*)} \qquad (\varepsilon > \varepsilon_c^*) \quad [14b]$$

$$\sigma^r = \sigma_{YS} - 5.6 f_{uc}\sqrt{\alpha}\,\mu_m\varepsilon^* \qquad (\varepsilon^* \le \varepsilon_c^*) \quad [15a]$$

$$\sigma^r = \sigma_{YS} - 5.6 f_{uc}\sqrt{\alpha}\,\mu_m\varepsilon_c^* + C\left(1 - \sqrt{f_{uc}}\right)\mu_m \sqrt{b\left(\frac{C_1}{\lambda} + \frac{C_2}{L}\right)(\varepsilon - \varepsilon_c^*)} \qquad (\varepsilon > \varepsilon_c^*) \quad [15b]$$

Assume that the net stress in the particles is close to zero when a tensile stress is just above yielding;[26] this leaves the particles under the sole effect of stresses arising from the plastic deformation. According to the preceding analysis, the stresses induced in the particles can be calculated by

$$\sigma_p = \frac{\sigma_b}{f_{uc}} = 5.6\sqrt{\alpha}\,\mu_m\varepsilon^* \qquad (\varepsilon^* \le \varepsilon_c^*) \quad [16a]$$

$$\sigma_p = 5.6\sqrt{\alpha}\,\mu_m\varepsilon_c^* + \frac{C\mu_m}{\sqrt{f_{uc}}} \sqrt{b\left(\frac{C_1}{\lambda} + \frac{C_2}{L}\right)(\varepsilon - \varepsilon_c^*)} \qquad (\varepsilon > \varepsilon_c^*) \quad [16b]$$

B. *Tensile Instability*

According to the Considère criterion, the global tensile instability of a material without internal damage occurs when the strain hardening rate ($d\sigma/d\varepsilon$) becomes equal to the flow stress, σ. Subsequently, the critical strain, ε_i, at which the global instability takes place, is equal to the strain-hardening exponent, n. The value of n is derived from a fit of the tensile data to the Hollomon equation ($\sigma = K\varepsilon^n$). The detailed procedure of deriving hardening exponent n is given in section III. Subsequent to the point (strain $\varepsilon_i = n$) of macroscopic instability, global necking occurs and the material deforms nonuniformly.

III. EXPERIMENTAL

A. *Materials and Heat Treatment*

Commercial unmodified Al-7 pct Si-0.3 to 0.7 pct Mg casting alloys (A356.0 and A357.0) were used in this study. Modification was achieved by adding Al-10 pct Sr master alloy to the unmodified melt just prior to degassing to achieve the target Sr level of 0.02 wt pct. The chemical compositions of the alloys are shown in Table I. Throughout this work, alloys are suffixed by "Sr" for strontium modified. Samples with a range of secondary dendrite arm spacing (SDAS) were produced by an end-chill sand casting procedure, details of which have been described elsewhere.[6,7,12]

To isolate the influence of porosity from other microstructural features on the tensile behavior, the castings were hot isostatically pressed (hipped) at 540 °C and a pressure of 100 MPa for 2 hours prior to T6 heat treatment. The T6 heat treatment included a solution treatment at 540 °C ± 3 °C for 20 hours, water quenching at room temperature, and a "preage" of 20 hours, at room temperature followed by an artificial aging for 6 hours at 170 °C ± 1 °C in a salt bath.

B. *Microstructure Characterization*

The microstructures of A356/357 alloys were quantified in terms of dendritic grain size, SDAS, and eutectic particle size (equivalent circle diameter) and aspect ratio. Quoted values for eutectic features are as measured on the polished sections of heat-treated samples, while grain size and SDAS were measured from as-cast samples. No attempt was yet made in this work to quantify Mg/Si precipitates.

To measure the grain size, the polished samples were anodized at 30 V and a current density of 1.6 mA/mm^2 for 30 seconds in a 2 pct solution of fluoroboric acid.[27] The anodized samples were then observed in an optical microscope under polarized light to reveal the grain structure. The grain size was measured using the intercept method. About 200 grains were measured for each determined point in the grain size plot (Figure 4).

The SDAS was quantified by identifying and measuring small groups of well-defined dendritic cells[28] on the screen of the image analyzer. The value of SDAS was then determined using SDAS = L/nM, where L is the length of the line drawn from edge to edge of the measured cells, M is the magnification, and n is the number of dendritic cells. The mean values of SDAS for each sample are the average of about 500 to 1000 dendrite arms.

The mean particle size (area equivalent circle diameter) and aspect ratio of each sample were quantified by measuring about 100 fields (200 times) of total 5000 to 10,000 particles. As the automated measurement of particle features depends somewhat on the gray level setting on the instrument, the detection level was set at about 60 pct of the aluminum gray level. It should be noted that no attempt was made to measure the orientation of eutectic particles because the particles are usually randomly oriented after

Table I. Chemical Composition of the Alloys (Weight Percent)

Alloy	Si	Mg	Fe	Ti	Sr	Cr, Cu, Mn, Ni, Zn, Zr
A356	6.8	0.39	0.13	0.13	<0.001	<0.01, each
A356Sr	7.0	0.41	0.14	0.13	0.02	<0.01, each
A357	6.9	0.69	0.14	0.09	<0.001	<0.01, each
A357Sr	6.8	0.64	0.14	0.09	0.02	<0.01, each

nondirectional solidification. Table II shows the mean particle size and aspect ratio as a function of SDAS. In both A356 and A357 alloys, the volume fraction of eutectic silicon is about 7 pct, while the amount of Fe-rich intermetallics depends on the Mg content in the alloy. In an A357 alloy with 0.7 wt pct Mg and 0.1 wt pct Fe, the amount of Fe-rich intermetallics (mostly π-phase particles) approached 1.4 vol pct.[10,11]

C. *Monotonic Tensile Testing*

The monotonic tensile specimens were flat with a cross section 5×4 mm^2 and gage length of 15 mm. Tensile testing was carried out on a screw-driven Instron machine (Canton, MA), at a strain rate of 10^{-3} s^{-1}. Stress-strain curves were obtained by attaching a knife-edge extensometer (12.5 mm) to the specimen gage length. The testing machine data logger was used to produce digital files for further analysis. Following testing, all fracture surfaces were examined in an optical stereo microscope and the samples that showed porosity or oxide defects in the fracture were rejected. The Young's modulus, 0.2 pct proof stress (referred to as yield strength), and elongation were determined from the digital files.

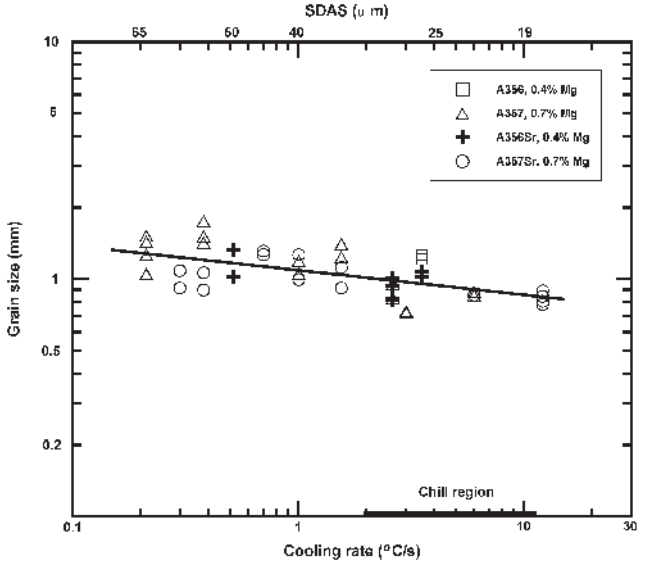

Fig. 4—Grain sizes of alloys A356/357 as a function of cooling rate during solidification.

D. *Multiloop Tensile and Compression Testing*

Multiloop tensile and compression testing was performed on samples with a gage region of 18-mm length and 8-mm diameter. A multiloop technique[29] was used (Figure 5). Basically, the samples were first deformed in tension up to a predetermined strain (about 0.003), unloaded and then compressed, deformed in tension to the next predetermined strain (with incremental of about 0.006), and cycled again. The process was continued up to fracture. Maximum compressive strain for each cycle was limited to about 0.003 to prevent buckling. The reverse flow stress for each loop was measured at a reverse offset strain of 0.002. Compared to the monotonic and single loop testing (Figure 5), the multiloop tensile and compression testing did not introduce additional hardening, indicating that the internal stress and Young's modulus determined at various plastic strains in the multiloop testing represent the plastic deformation behavior in monotonic tensile testing.

In this work, the Young's modulus E at a given plastic strain was measured from the multiloop tensile and compression curves, by linearly fitting the initial portion of the tension curve. There is a difference in initial modulus between tests due to the variation of alloy microstructures. A normalized modulus, E/E_0, and a damage parameter, $D = 1 - E/E_0$, where E is the modulus at a given plastic strain and E_0 is the initial unstrained modulus, were computed for each test.

E. *Determination of Strain-Hardening Exponent, n*

The strain-hardening exponent n value in the Hollomon equation ($\sigma = K\varepsilon^n$) was determined from a linear fit to the log true stress–log true strain data (from the monotonic tensile testing) over a strain range from about 0.01 to the instability point, as shown in Figure 6.

IV. RESULTS

A. *Strain-Hardening Behavior*

Figure 7 shows the influence of Mg content on the flow behavior in both unmodified and Sr-modified alloys. Increasing Mg content (matrix strength) increases the strain-hardening rate at low strains, leading to a higher yield strength. At larger strains, however, the degree of hardening becomes similar for both alloys. This indicates that the strain-hardening behavior at large strains is not significantly affected by matrix strength.

Table II. Eutectic Particle Size (Area Equivalent Circle Diameter, ECD) and Aspect Ratio

Cooling Rate (°C/s)	SDAS (μm)	Mean ECD (μm)				Mean Aspect Ratio			
		A356	A356Sr	A357	A357Sr	A356	A356Sr	A357	A357Sr
0.20	66	6.43	—	—	—	2.68	—	—	—
0.34	56	6.35	3.52	7.30	3.58	2.63	1.55	2.25	1.62
0.41	52	—	3.35	—	—	—	1.53	—	—
0.52	48	5.52	—	6.68	3.42	2.43	1.53	2.14	1.61
0.93	40	5.06	3.26	5.90	3.41	2.17	1.52	2.05	1.59
1.44	35	—	3.18	—	—	—	1.52	—	—
2.36	30	4.94	—	5.63	3.36	1.89	—	1.90	1.56
3.58	26	4.78	3.15	4.89	3.33	1.96	1.51	1.85	1.55
12.94	17	3.81	2.83	4.13	3.09	1.73	1.50	1.74	1.53

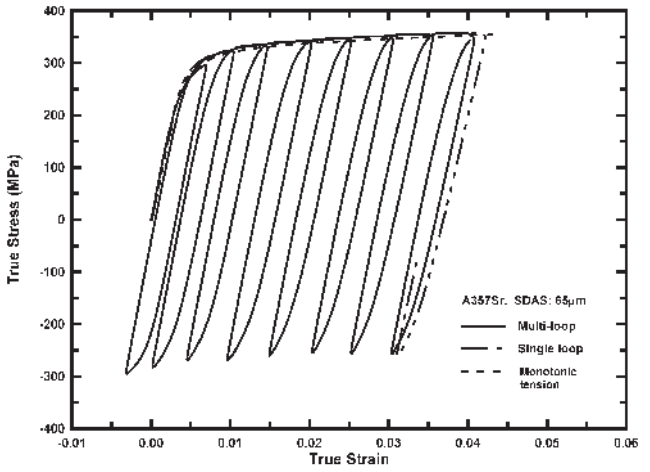

Fig. 5—Comparison of single, multiloop, and monotonic stress-strain curves.[16]

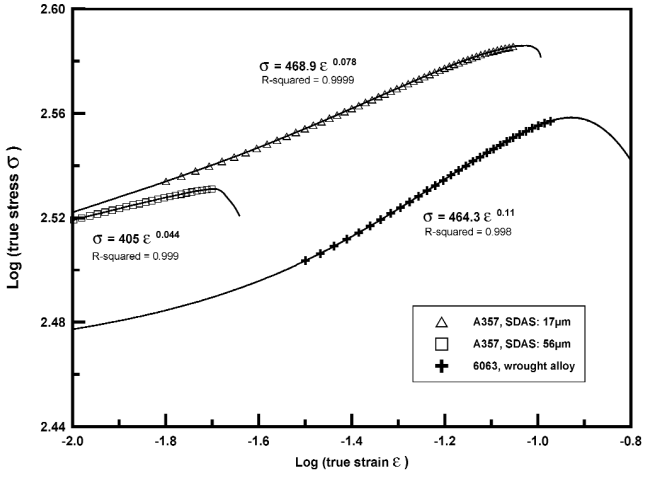

Fig. 6—Determination of n values for alloys by linear fit to the log true stress–log true strain curves. All alloys were in the T6 condition.

The effect of particle aspect ratio on the strain-hardening behavior is shown in Figure 8. Increasing particle aspect ratio in both A356 and A357 alloys increases the yield stress. However, at large strains (>1 pct), the effect of the particle aspect ratio becomes much less pronounced. Figure 9 shows the effect of particle aspect ratio on the strain-hardening rate at the applied strain of 0.0015. For a given Mg content, the strain-hardening rate increases with the particle aspect ratio, while at a given aspect ratio, the higher Mg content alloy exhibits a higher hardening rate. The predicted hardening rates at the applied strain of 0.0015 using the current dispersion hardening model [Eq. (14a)] are comparable to those measured.

In contrast to the particle aspect ratio, the SDAS has little influence on the flow behavior at low strains. At large strains, the effect of SDAS on the strain hardening becomes evident. Figure 10 compares the flow curves of an Sr-modified alloy with large SDAS and small SDAS. Figure 11 illustrates the influence of SDAS on the strain-hardening rate at an applied strain of 0.02 to 0.025. Decreasing SDAS enhances the strain hardening at large strains. For alloys with constant eutectic

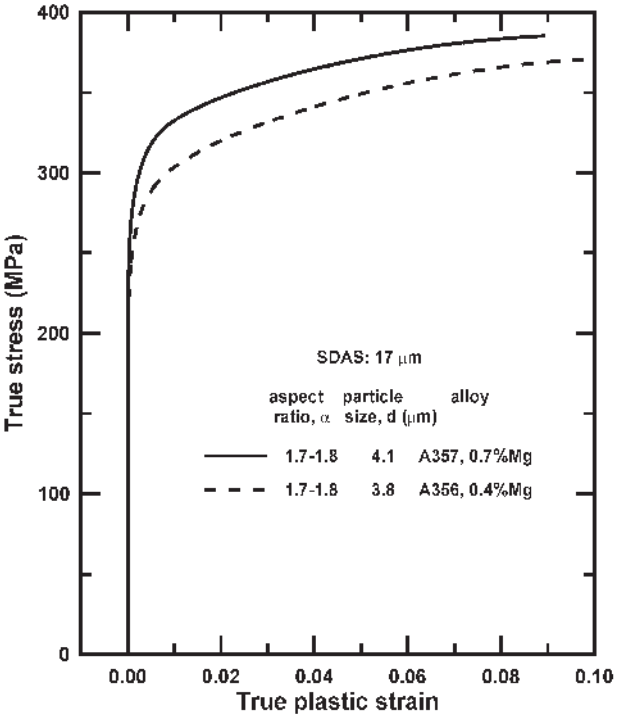

(*a*)

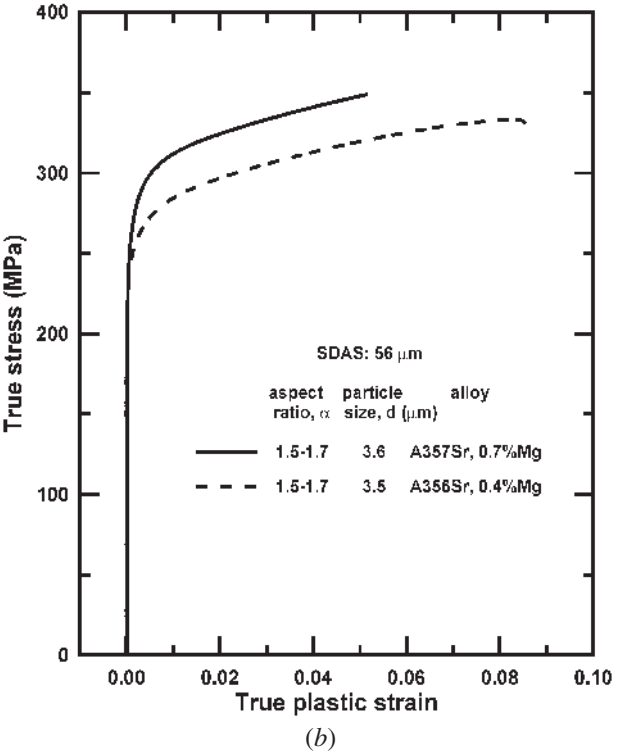

(*b*)

Fig. 7—True stress–true plastic strain curves showing the effect of Mg content on the flow behavior of (*a*) unmodified and (*b*) Sr-modified alloys A356/357 (T6 heat treatment).

particle aspect ratio, the strain-hardening rate increases with decreasing SDAS. The prediction of hardening rates using Eq. [14b] is in good agreement with the experimental data.

Figure 12 shows the strain-hardening exponent (n) values, which were determined from the monotonic tensile true

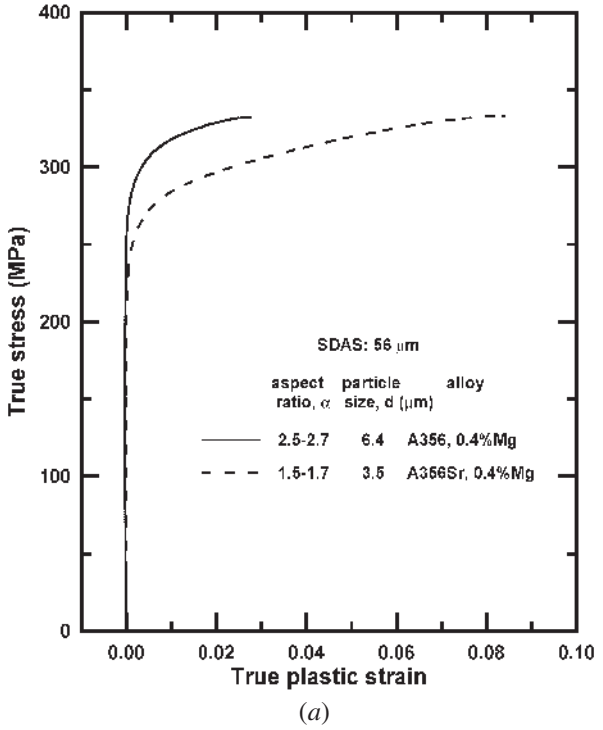

(*a*)

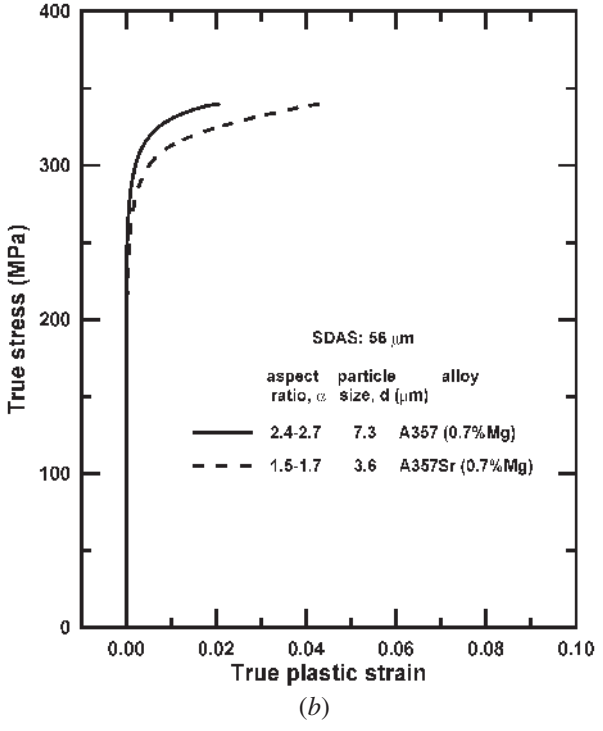

(*b*)

Fig. 8—True stress–true plastic strain curves showing the effect of particle aspect ratio on the flow behavior of (*a*) A356 alloys and (*b*) A357 alloys.

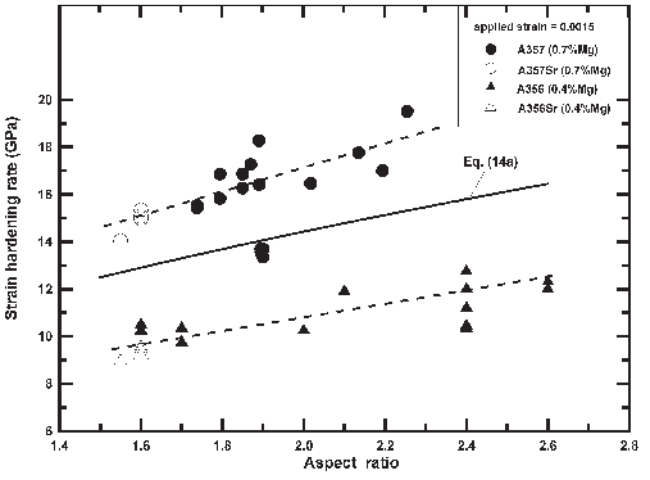

Fig. 9—The strain-hardening rate as a function of particle aspect ratio, measured at a plastic strain of 0.0015.[16] The dashed lines are the least-squares best fit. The solid line is based on the model predictions.

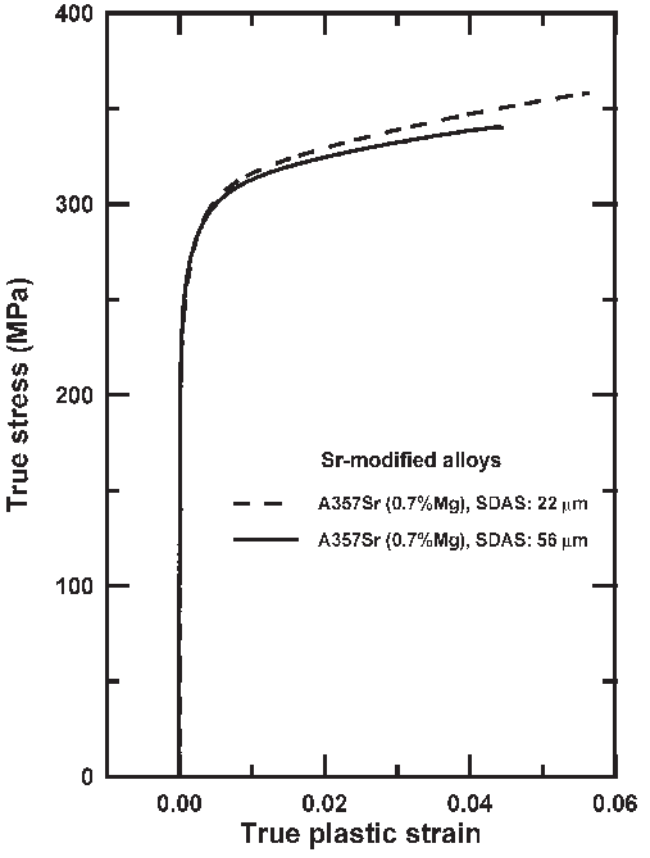

Fig. 10—True stress–true plastic strain curves showing the effect of SDAS on the flow behavior of an Sr-modified alloy A357.

stress and true strain curves, as a function of SDAS. Increasing SDAS decreases the strain-hardening exponents, especially in the unmodified alloys. Strontium modification of eutectic silicon particles increases the strain-hardening exponents. Increasing Mg content in the alloy significantly reduces the strain-hardening exponent, especially in the Sr-modified alloy A357.

B. *Internal Stresses Induced in the Eutectic Particles*

Figures 13 and 14 show the development of internal stresses in the eutectic particles during plastic deformation. Initially, the particle stresses increase very rapidly at low strains (<1 pct), then accumulate at a much lower rate at large strains due to the onset of plastic relaxation and particle cracking. It should be noted that some compressive stresses have been measured

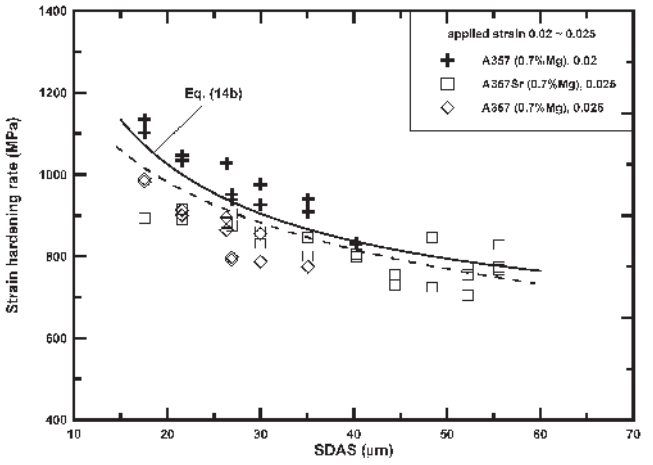

Fig. 11—The strain-hardening rate measured at the applied plastic strains between 0.02 and 0.025, as a function of SDAS for samples with a particle aspect ratio between 1.5 and 1.9. The dashed line is a least-squares best fit. The solid line represents values predicted by the model.

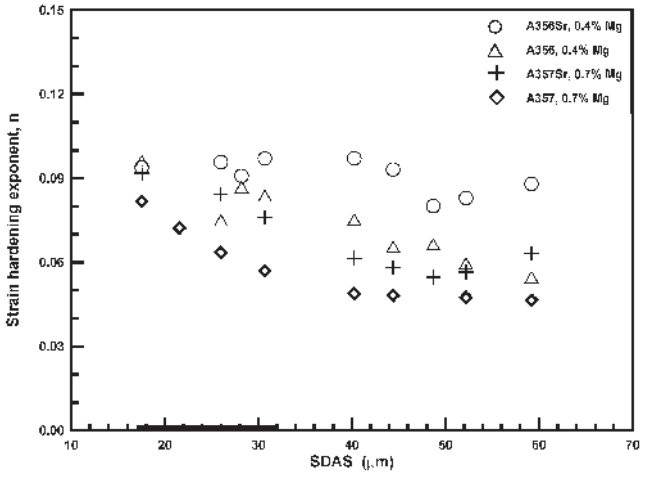

Fig. 12—Strain-hardening exponent, *n*, as a function of SDAS for alloys A356 and A357, both unmodified and Sr-modified.

in the eutectic particles before the plastic deformation. This so-called 'misfit stress' was caused by the difference in the thermal expansion coefficient between eutectic particles and aluminum matrix,[26] which puts the particles under a compressive stress of the order of the matrix yield stress.

The influence of particle aspect ratio on the development of internal stresses with the applied strains can be interpreted from the Figure 13. For the unmodified alloys with large and elongated particles, the particle stresses increase very rapidly and approach 800 MPa at very low strains compared to the alloys with small and round particles, such as in the Sr-modified alloys. The calculated values from Eq. [16] are in good agreement with the results inferred from the multiloop Bauschinger effect measurements.

For alloys with fine eutectic particles, for instance, in the Sr-modified alloys, the development of particle stresses shows some dependence on the SDAS. As can be seen in Figure 14, the particle stresses in the small SDAS structure saturate at a higher value in comparison with the large SDAS alloys. It is also noted that the experimental data suggest a net effect of SDAS on the particle stresses in the order of the predicted value.

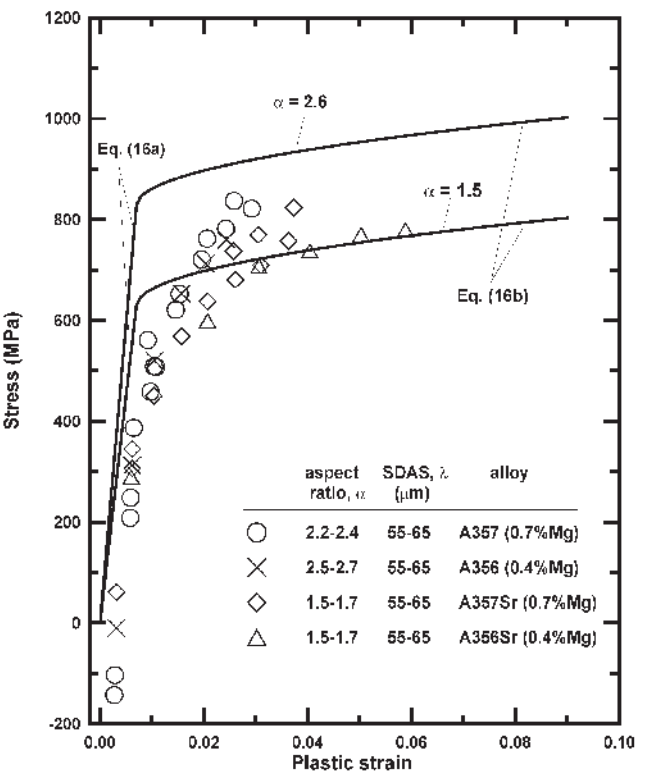

Fig. 13—The (tensile) stresses in the particles as a function of plastic strain for materials (T6 heat treatment) with the same SDAS but different particle aspect ratios.

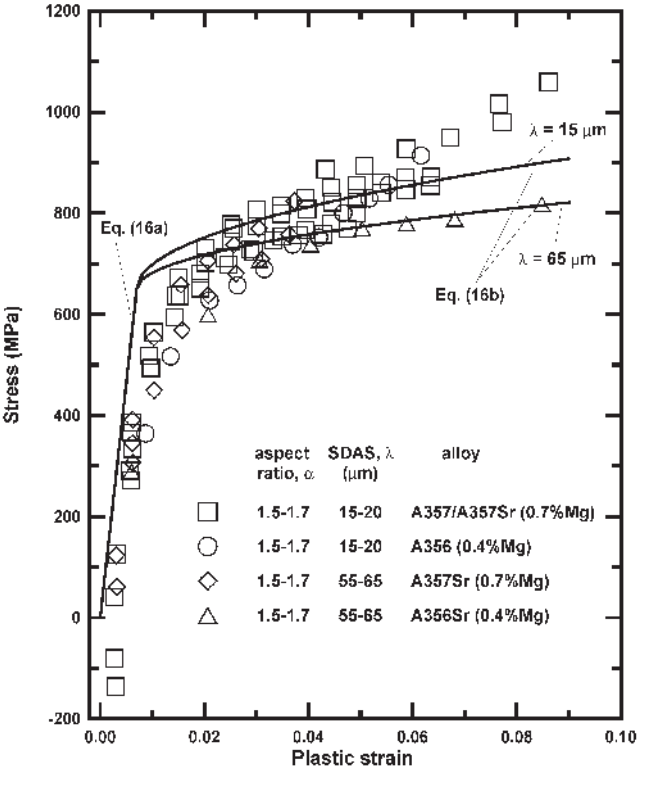

Fig. 14—The (tensile) stresses in the particles as a function of plastic strain for materials (T6 heat treatment) with similar particle aspect ratio but different SDAS.

C. *Damage Evolution by Particle Cracking*

As shown in Section B, the particle stresses are strongly dependent on the plastic strain of the surrounding matrix. The larger the plastic strain, the higher the particle stresses. When the particle stress approaches the particle fracture strength, the particle cracks. Figure 15 shows the nature of the silicon and Fe-rich intermetallic particle cracking in the A357 alloy. The large and elongated particles crack first due to the high internal stresses developed. It is also noted that the fracture in the cracked particles is normal to the global tension axis, even when this was the longest fracture path in the particles (as indicated by "A" in Figure 15(b)), similar to findings reported by Gangulee and Gurland[4] and by Frederick and Bailey.[3] This indicates that cracking occurs due to the development of tensile stresses in the particles.

Particle cracking leads to an apparent decrease of Young's modulus for the alloys during plastic deformation. Figure 16 shows the evolution of Young's modulus (and in turn the damage) as a function of plastic strain. In the coarse microstructure (SDAS: 55 to 65 μm), the damage rates of the unmodified A356 and A357 alloys and the Sr-modified A357 alloy are quite similar and are higher than that of the Sr-modified A356 alloy. This suggests that at the same amount of plastic strain, more voids and microcracks (due to particle cracking) form in the A357 alloy (both the unmodified and the Sr-modified structures) and the unmodified A356 alloy, and this leads to the earlier failure of these alloys. At fracture strain, all four alloys have a similar amount of damage and loss of Young's modulus (10 to 12 pct). This indicates that fracture occurs when the alloy develops a critical amount of damage, regardless of the Mg content and state of modification.[9,11,30]

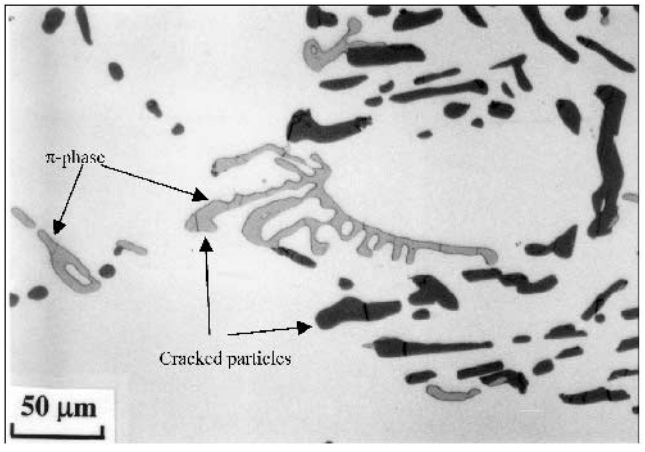

(*a*)

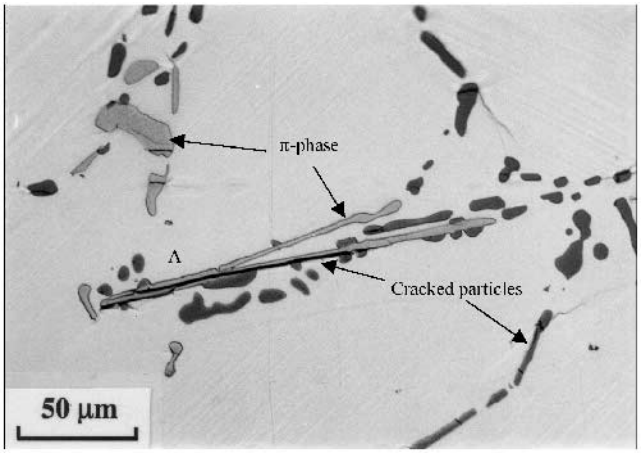

(*b*)

Fig. 15—Micrographs showing particle cracking in an A357 alloy (applied strain 2.4 pct, T6 heat treatment, SDAS: 56 μm): (*a*) inside specimen and (*b*) on the surface of specimen. The tensile axis is horizontal in (a) and vertical in (b).

D. *Tensile Instability*

Figure 17 illustrates the tensile instability behavior of four alloys with different SDAS values. For all alloys studied, the strain-hardening curves do in fact intersect the flow curves prior to failure of the alloys. However, the intersection points are all offset from the global instability strains as would be predicted by the Hollomon equation ($\sigma = K\varepsilon^n$). In alloys with large SDAS, the failure takes place prior to the occurrence of global tensile instability ($\varepsilon_f < n$), suggesting the high damage rate by particle cracking. In the small SDAS microstructures, the global instability occurs at strains well below the true fracture strains ($\varepsilon_f > n$). This indicates that the damage accumulation rate is low and there is still a postnecking damage (particle cracking). Therefore, the failure criteria in this group of alloys should be derived from the damage accumulation regardless of the fineness of the microstructure.

V. DISCUSSION

A. *Strain-Hardening Behavior*

The results in Figures 7 through 11 indicate that both particle aspect ratio and SDAS play an important role in the strain-hardening process in these alloys, as reported previously for the A356 alloy[7] and A357 alloy.[16] Figure 7

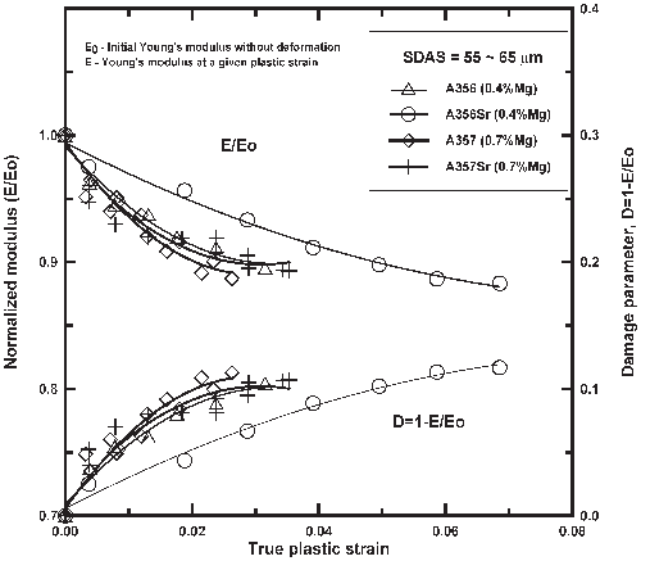

Fig. 16—Damage evolution of four alloys (T6 heat treatment), reflected in the modulus loss under deformation.

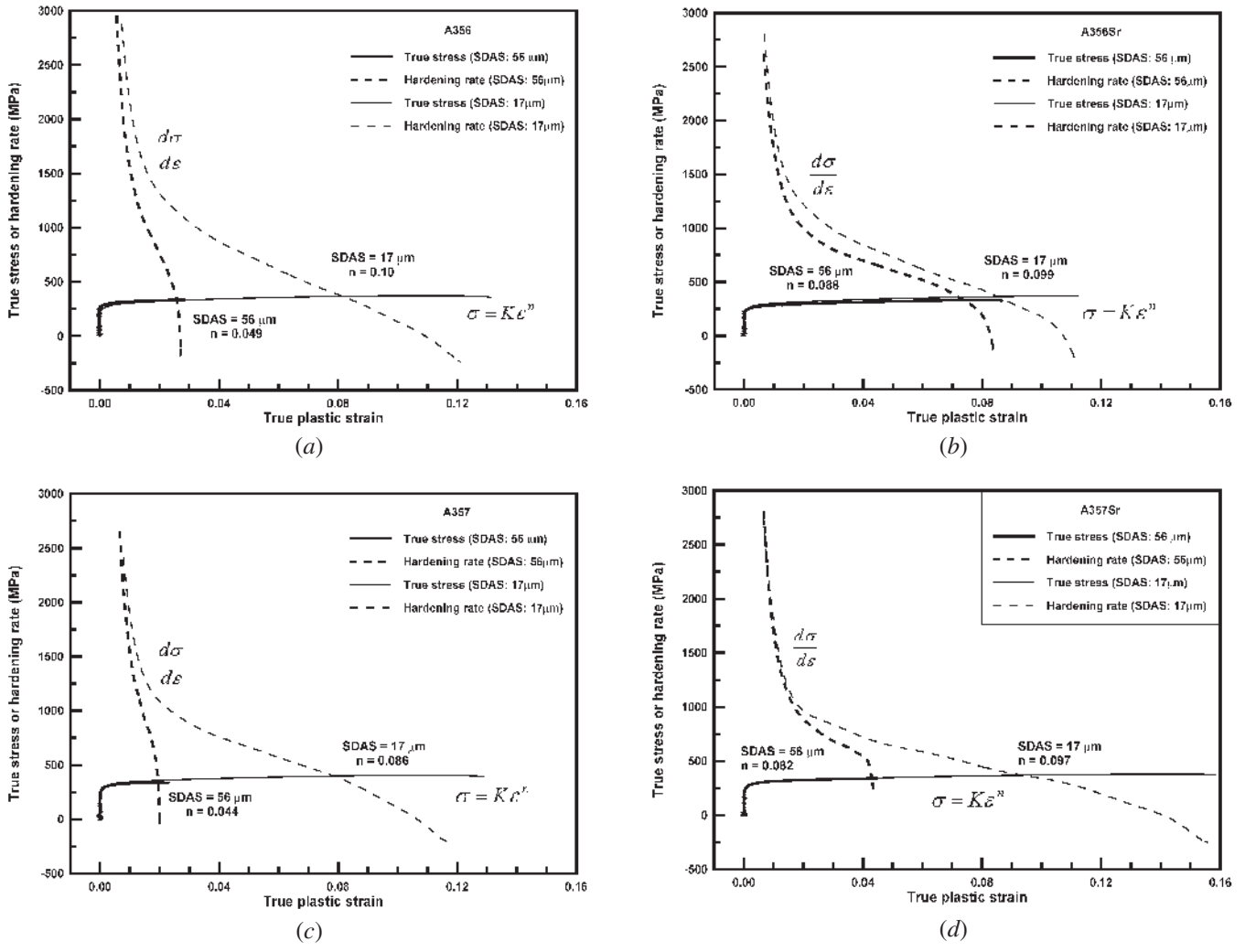

Fig. 17—Tensile instability plots for alloys (*a*) unmodified A356, (*b*) Sr-modified A356, (*c*) unmodified A357, and (*d*) Sr-modified A357.

also shows a strong effect of the Mg content on the hardening rate at low strains. By way of comparison, the strain-hardening rate at a strain of 0.0015 is of the order of 16 GPa for A357 alloy (0.7 pct Mg) and 11 GPa for A356 alloy (0.4 pct Mg), respectively.

Since the silicon content of the two casting alloys is similar (as is the silicon particle aspect ratio), the difference between them can only be attributed to the different Mg content. To understand the effect of Mg on the hardening rate of the casting alloys, the different contributions to the strain hardening need to be considered. At low strains, plastic deformation results in the accumulation of Orowan loops piled up around the reinforcing eutectic particles. Deformation is highly inhomogeneous and the flow stress increases linearly with the matrix plastic strain (linear hardening regime).[7,14,15,21] At increasing strains, the stresses in the piled-up dislocations around the eutectic particles become high enough to induce cross-slip and secondary slip. Continued plastic straining then results in strain hardening at a much reduced rate due to the formation of a forest of dislocations near the tip of the reinforcing particles (parabolic hardening regime).[14,15,21] The transition between the two regimes is likely to be controlled by the relative strength of the matrix.[29]

Increasing Mg content has two effects on the strain-hardening rate at low strains. One is that increasing Mg increases the matrix strength by increasing the number of Mg/Si precipitates and reducing the distance between precipitates. This leads to a stronger resistance to plastic relaxation and the cross-slip of dislocations. The other effect is an increase in the volume fraction and size of Fe-rich intermetallics, due to the formation of more π phase with Mg additions over 0.4 pct.[10,31,32] As a result, the strain-hardening rate is increased with the Mg content at low plastic strain.

The increased Mg content seems to have a negligible effect on the strain-hardening behavior at large strains (>0.02), which is consistent with the present picture since hardening in the parabolic regime results from the accumulation of dislocations in the cell and grain boundaries in the matrix. The influence of matrix strength on the strain hardening depends on the nature of the Mg/Si precipitates in aluminum and the degree of damage accumulation. Shearable precipitates lead to a small Bauschinger effect, the order of that of pure aluminum,[7,33] while impenetrable precipitates result in a large Bauschinger effect, and in some cases, inflected Bauschinger loops.[7,33–35] In the alloys A356 and A357 used in this work, T6 aged to near peak hardness, the precipitates

were sheared on yielding (refer to the well-defined straight slip bands observed in Figures 1 and 2).[2] Thus, a small contribution to the hardening should be expected from the matrix alone at large strains.

B. *Stresses in the Particles*

Application of Eq. [16] to the multiloop tensile and compression test results allows the calculation of particle stresses during plastic deformation. This was done in Figures 13 and 14. The results indicate that particle stresses can be very high after relatively small strains for all microstructures. Elongated particles seem to accumulate stresses at a faster rate, as shown in Figure 13. This conclusion is supported by the fact that the elongated particles tend to crack earlier.[8,9,11] Figure 14 also indicates that for a constant particle aspect ratio, small SDAS microstructure tends to produce slightly higher particle stresses in comparison with large SDAS microstructure. To understand why small SDAS with higher particle stresses still yields higher ductility compared with large SDAS for a constant and small particle aspect ratio, the damage process of the materials needs to be considered. The damage process of alloys A356 and A357 consists of three mixed events: particle cracking, microcrack formation and growth, and local linkage of microcracks.[12] The ductility of the alloys is determined by the strain necessary to produce a critical amount of voids by particle cracking and the strain needed for the voids to grow to a critical size at which point a local shear instability causes macroscopic fracture.[30,36] The particle cracking rate depends not only on the particle stress but also on the fracture strength of the particles. A larger volume particle induces lower strengths and higher variability because of a higher probability of having surface and volume defects. The void growth strain depends on the volume fraction of the particles. It becomes negligible and the total ductility is solely determined by the nucleation strain, at volume fraction of 16 pct or higher, when the particles are close enough to each other so that the shear instability develops as soon as the voids are nucleated.[36] In the alloys used in this work, the density of particles in the interdendritic clusters, as in the large SDAS (Figure 1) is fixed by the eutectic reaction at about 12 pct, which is close to the critical value (16 pct) and hence the growth strain can be expected to be very small. At small SDAS, however, the dendritic boundaries become diffuse and the particles are no longer clustered (Figure 2). The local and average volume fractions of particles become similar at about 7 pct, which is well below the critical 16 pct, and an increased ductility thus results.

The compression stress (negative stress) observed at very low strains in Figures 13 and 14 is an indication of residual stress in the particles, resulting from the difference in the thermal expansion coefficient between particles and aluminum matrix during heat treatment.[26,29]

C. *Damage by Eutectic Particle Cracking*

The decrease in Young's modulus with increasing plastic strain is most likely caused by the progressive cracking of particles. The apparent modulus, E_c, of a cracked body containing penny-shaped cracks is related to the modulus, E_o, of the material by[37]

$$\frac{E_o}{E_c} = 1 + \frac{16(1 - v^2)N_c d_c^3}{3} \qquad [17]$$

where d_c is the diameter of the cracks, *v is Poisson's ratio*, and N_c is the number of cracks per unit volume. This equation cannot at once be used for the present experiments because the cracks are formed in stiff second-phase particles. As a first approach, we can estimate the modulus of Al stiffened by 7 wt pct Si[26] to be 75 GPa, compared to 69 GPa for Al. Suppose, for example, that 20 pct of the silicon particles crack: this corresponds to about 45 pct of the total area fraction of Si particles.[8,9,11] The modulus loss is then ~3 GPa due to loss of stiffening by the Si together with a further loss according to Eq. [17]. Assuming that 20 pct of silicon particles are cracked, the number of cracks per cubic meter can be estimated by $N_c = 20$ pct $N = 20$ pct $\frac{f}{V} = 20$ pct $\frac{6f}{\pi d^3}$, where V and d are the mean volume (m^3)and mean size of total particles, respectively. The term f is the volume fraction of total particles in the alloy. For the slowly solidified A357 unmodified alloy (SDAS: 56 μm), d is about 6.5 μm and d_c is about 9.0 μm.[9,11] Accordingly, Eq. [17] gives the further loss as 3 GPa, giving a total loss of 6 GPa, or 8 pct of the initial modulus of 75 GPa. This value can be seen to correspond with the order of magnitude measured by experiment (Figure 16).

D. *Tensile Instability*

The final failure of an alloy is controlled by both global and local instability. In the coarse microstructure (large SDAS), the large and elongated particles are densely grouped in either cell or grain boundaries and thus local instability, due to the cluster of cracked particles, dominates the fracture. As shown in Figure 18, the ratio of tensile instability

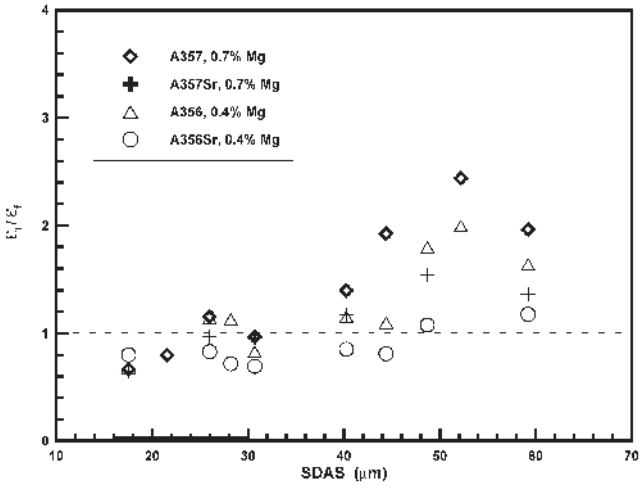

Fig. 18—The ratio of tensile instability ε_i to fracture strain ε_f of alloys as a function of SDAS. $\varepsilon_i/\varepsilon_f > 1$ indicates that local fracture governs tensile instability, while $\varepsilon_i/\varepsilon_f < 1$ indicates more uniform damage accumulation where tensile instability occurs at the onset of macroscopic necking.

($\varepsilon_i = n$) to fracture strain (ε_f) is larger than 1 $\left(\frac{\varepsilon_i}{\varepsilon_f} > 1\right)$, indicating that the alloy fails prior to the global instability taking place. In the finer structure (small SDAS), the small silicon and Fe-rich intermetallic particles are more homogeneously spaced. They crack uniformly and particularly at a lower cracking rate. As shown in Figure 17, there is substantial postuniform deformation in the samples (that is, $\frac{\varepsilon_i}{\varepsilon_f} < 1$, Figure 18). This nonuniform deformation continues until a value of critical strain is achieved. This critical strain, typically close to the fracture strain, is the point at which a certain amount of damage by particle cracking is achieved. In this case, the global area or number fraction of cracked particles can be used as a fracture criterion.

VI. CONCLUSIONS

The plastic deformation behavior of A356 and A357 alloys has been studied as a function of SDAS, Mg content, and eutectic particle aspect ratio for both unmodified and Sr-modified structures. The following conclusions can be drawn from this work.

1. During plastic deformation, alloys with elongated particles or high Mg content show high strain-hardening rate at low strains for both unmodified and Sr-modified alloys. At large strains, a higher hardening rate is observed for alloys with fine dendrites.
2. For all alloys studied, the average internal stresses increase very rapidly at small strains and gradually saturate at large strains. For a given SDAS, the particle internal stresses saturate at a higher value in alloys with elongated eutectic particles or higher Mg content. At large strains and constant particle aspect ratio, alloys with the smaller SDAS show higher internal stresses.
3. The higher the internal stresses, the higher the damage rate of particle cracking and thus the lower the Young's modulus during plastic deformation.
4. Current models for dispersion hardening account well for the SDAS and in particular the particle aspect ratio on the tensile behavior. The calculated strain-hardening rate and the internal particle stresses agree well with the results inferred from the experimental measurements.
5. The fracture strain of alloys A356/357 corresponds to the critical amount of damage by particle cracking locally or globally, irrespective of the fineness of the microstructure. In the coarse structure, this critical amount of damage is easily reached, due to the clusters of large and elongated particles, leading to alloy fracture before global necking. However, in the alloy with the small SDAS, the critical amount of damage is postponed until global necking takes place, due to the small and round particles with much lower damage rate.

ACKNOWLEDGMENTS

The author expresses his sincere gratitude to Dr. C.H. Cáceres (CAST) and Dr. J.R. Griffiths (CSIRO) for their invaluable discussion through this work. Support from the Australian Education Department OPRS Program, the Australian Government's Co-operative Research Center Program (CAST), Boeing Commercial Airplane Group, and Comalco Research Center is gratefully acknowledged.

REFERENCES

1. G.A. Edwards, K. Stiller, G.L. Dunlop, and M.J. Couper: *Mater. Sci. Forum*, 1996, vols. 217–222, pp. 713-18.
2. Q.G. Wang and C.H. Cáceres: *Mater. Sci. Eng.*, 1998, vol. A241, pp. 72-78.
3. S.F. Frederick and W.A. Bailey: *Trans. TMS-AIME*, 1968, vol. 242, p. 2063.
4. A. Gangulee and J. Gurland: *Trans. TMS-AIME*, 1967, vol. 239, pp. 269-72.
5. C.W. Meyers, A. Saigal, and J.T. Berry: *AFS Trans.*, 1983, vol. 91, pp. 281-88.
6. C.H. Cáceres, C.J. Davidson, and J.R. Griffiths: *Mater. Sci. Eng. A*, 1995, vol. 197, pp. 171-79.
7. C.H. Cáceres, J.R. Griffiths, and P. Reiner: *Acta Mater.*, 1996, vol. 44, pp. 15-23.
8. C.H. Cáceres and J.R. Griffiths: *Acta Mater.*, 1996, vol. 44, pp. 25-33.
9. Q.G. Wang, C.H. Cáceres, and J.R. Griffiths: *AFS Trans.*, 1998, vol. 106, pp. 131-36.
10. C.H. Cáceres, C.J. Davidson, J.R. Griffiths, and Q.G. Wang: *Metall. Mater. Trans. A*, 1999, vol. 30A, pp. 2611-18.
11. Q.G. Wang, C.H. Cáceres, and J.R. Griffiths: *Metall. Mater. Trans. A*, 2003, vol. 34A, pp. 2901-12.
12. Q.G. Wang: *Metall. Mater. Trans. A*, 2003, vol. 34A, pp. 2887-99.
13. C. Verdu, H. Cercueil, S. Communal, P. Sainfort, and R. Fougeres: *Mater. Sci. Forum*, 1996, vols. 217-222, pp. 1449-54.
14. L.M. Brown and W.M. Stobbs: *Phil. Mag.*, 1971, vol. 23, pp. 1185-99.
15. L.M. Brown and W.M. Stobbs: *Phil. Mag.*, 1971, vol. 23, pp. 1201-33.
16. Q.G. Wang and C.H. Cáceres: *Mater. Sci. Eng. A*, 1997, vols. A234–A236, pp. 106-09.
17. J.D. Embury: *Metall. Trans. A*, 1985, vol. 16A, pp. 2191-200.
18. G.D. Moan and J.D. Embury: *Acta Metall.*, 1979, vol. 27, p. 903.
19. R. Sowerby, D.K. Uko, and Y. Tomita: *Mater. Sci. Eng. A*, 1979, vol. 41, pp. 43-58.
20. J.D. Embury: *Mater. Forum*, 1987, vol. 10(1), pp. 27-32.
21. M.F. Ashby: *Strengthening Methods in Crystals*, A. Kelly and R.B. Nicholson, eds., Elsevier, Amsterdam, 1971, pp. 137-92.
22. L.M. Brown and D.R. Clarke: *Acta Metall.*, 1975, vol. 23, pp. 821-30.
23. L.M. Brown: *Acta Metall.*, 1973, vol. 21, pp. 879-85.
24. Y. Brechet, J.D. Embury, S. Tao, and L. Luo: *Acta Metall. Mater.*, 1991, vol. 39, pp. 1781-86.
25. N. Hansen: *Acta Metall.*, 1977, vol. 25, pp. 863-69.
26. R.W. Coade, J.R. Griffiths, B.A. Parker, and P.J. Stevens: *Phil. Mag.*, 1981, vol. A44 (2), pp. 357-72.
27. R.S. Chappell, T.A. Hughes, and G. Pollard: *Metallography*, 1970, vol. 3, pp. 235-37.
28. P.N. Crepeau: *AFS Trans.*, 1996, vol. 103, pp. 361-66.
29. S.F. Corbin and D.S. Wilkinson: *Acta Metall. Mater.*, 1994, vol. 42 (4), pp. 1311-18.
30. C.H. Cáceres: *Aluminum Trans.*, 1999, vol. 1 (1), pp. 1-13.
31. Q.G. Wang and C.J. Davidson: *J. Mater. Sci.*, 2001, vol. 36, pp. 739-50.
32. J.A. Taylor, D.H. St John, J. Barresi, and M.J. Couper: *Mater. Sci. Forum*, 2000, vols. 331–337, pp. 277-82.
33. R.E. Stoltz and R.M. Pelloux: *Metall. Trans. A*, 1976, vol. 7A, p. 1295.
34. T.K. Hidayetoglu, P.N. Pica, and W.L. Haworth: *Mater. Sci. Eng.*, 1985, vol. 73A, p. 65.
35. A. Aran, M. Demirkol, and A. Karabulut: *Mater. Sci. Eng.*, 1987, vol. 89A, p. 35.
36. D.J. Lloyd: *Acta Metall. Mater.*, 1991, vol. 39, pp. 59-71.
37. J.R. Griffiths: CSIRO Manufacturing and Infrastructure Technology, Kenmore, QLD, Australia, private communication, 1997.